Distributed Bilayer Photovoltaics Based on Nematic Liquid Crystal Polymer Networks

Wing C. Tsoi,[†] Mary O'Neill,*[,†] Matthew P. Aldred,[‡] Stuart P. Kitney,[‡] Panagiotis Vlachos,[‡] and Stephen M. Kelly*[,‡]

Departments of Physics and Chemistry, University of Hull, Cottingham Road, Hull HU6 7RX, U.K.

Received June 29, 2007. Revised Manuscript Received August 31, 2007

We discuss a liquid crystal composite approach to provide a distributed interface to vertically separate electron-donating and electron-accepting films in an organic photovoltaic device. Two different methods are used to prepare a nematic liquid crystal polymer network with a porous surface and electron-donating properties. This is infilled with an electron-accepting organic semiconductor to form a bilayer device. The interface is diffuse rather than localized so that more photogenerated excitons can reach it to generate charge before they recombine. Photoinduced absorption of a blend of the donor and acceptor materials confirms that excitons dissociate at the heterointerface. The spatial features of the diffuse interface are examined by Fourier analysis of topographic images. We find a correlation between the in-plane spatial frequencies of the interface and photovoltaic device performance. The device performance is investigated as a function of input irradiance. Any charge combination is monomolecular rather than bimolecular, and the monochromatic power conversion efficiency varies between 0.8% and 0.3% with input irradiance. Equivalent circuit analysis shows that this is limited by a high series resistance, a blocking contact, and nonoptimized spatial features of the porous interface.

I. Introduction

We have recently proposed the use of liquid crystalline gels as a new way to tackle one of the key challenges for organic photovoltaics, the provision of a distributed interface to vertically separate electron-donating [ED] and electron-accepting [EA] materials.[1] Unlike inorganic semiconductors, the exciton binding energy of organic semiconductors is very high so that an electric field is insufficient to efficiently separate the photogenerated excitons into free electrons and holes. Instead charge separation normally occurs at a heterointerface by trapping the hole and electron, respectively, in the ED and EA materials, whose energy levels are offset by more than the exciton binding energy.[2,3] The diffusion length of the exciton before recombination is very short so that distributed interfaces are often used to maximize charge separation.[4−7] Ideally the ED and EA materials should be vertically separated to ensure that electron and holes arrive at different electrodes only.[8−11] Liquid crystal gels contain phase-separated droplets of liquid crystals (LCs) in a cross-linked polymer network.[12] They can be formed by depositing a thin film containing a homogeneous blend of a polymerizable LC and a nonpolymerizable LC. The polymerizable LC, or so-called reactive mesogen, has polymerizable terminal groups which cross-link on irradiation with ultraviolet light, resulting in the photoinduced phase separation of the cross-linked and nonpolymerizable components of the blend.[1] In our original photovoltaic device both components of the gel have ED semiconducting properties, and the nonpolymerized droplets were removed by washing in an appropriate solvent. This results in an ED layer with a porous surface with nanometer sized grooves, which provided a large area interface to an EA layer, which was deposited on top of the porous ED layer by solution processing to form the photovoltaic device. Ideally, as illustrated in the reference, the porous surface should penetrate most of the active layer of the device to ensure all photogenerated excitons reach an interface before recombination.[1]

The application of polymerizable calamitic [rigid-rod-like] liquid crystal composites [reactive mesogens] to organic photovoltaics offers many attractive and distinct features. Unlike main-chain polymer blends, which phase separate spontaneously on solution processing, thin films of LC

* Corresponding author phone: +441482465246; e-mail: m.oneill@hull.ac.uk (M.O.); phone: +441482465219; e-mail: s.m.kelly@hull.ac.uk (S.M.K.).

[†] Department of Physics.

[‡] Department of Chemistry.

(1) Carrasco-Orozco, M.; Tsoi, W. C.; O'Neill, M.; Aldred, M. P.; Vlachos, P.; Kelly, S. M. *Adv. Mater.* **2006**, *18*, 1754.
(2) Tang, C. W. *Appl. Phys. Lett.* **1986**, *48*, 183.;
(3) Xue, J. G.; Uchida, S.; Rand, B. P.; Forrest, S. R. *Appl. Phys. Lett.* **2004**, *84*, 3013.
(4) Halls, J. J.; Walsh, C. A.; Greenham, N. C.; Marseglia, E. A.; Friend, R. H.; Moratti, S. C.; Holmes, A. B. *Nature* **1995**, *376*, 498.
(5) Yu, G.; Heeger, A. J. *J. Appl. Phys.* **1995**, *78*, 4510.
(6) Kim, Y.; Cook, S.; Tuladhar, S. M.; Choulis, S. A.; Nelson, J.; Durrant, J. R.; Bradley, D. D. C.; Giles, M.; McCulloch, I.; Ha, C. S.; Ree, M. *Nat. Mater.* **2006**, *5*, 197.
(7) Reyes-Reyes, M.; Kim, K.; Carroll, D. L. *Appl. Phys. Lett.* **2005**, *87*, 083506.
(8) Granström, M.; Petritsch, K.; Arias, A. C.; Lux, A.; Andersson, M. R.; Friend, R. H. *Nature* **1998**, *395*, 257.
(9) Arias, A. C.; Corcoran, N.; Banach, M.; Friend, R. H.; MacKenzie, J. D.; Huck, W. T. S. *Appl. Phys. Lett.* **2002**, *80*, 1695.
(10) Chen, L. C.; Godovsky, D.; Inganäs, O.; Hummelen, J. C.; Janssens, R. A. J.; Svensson, M.; Andersson, M. R. *Adv. Mater.* **2000**, *12*, 1367.
(11) Drees, M.; Premaratne, K.; Graupner, W.; Heflin, J. R.; Davis, R. M.; Marciu, D.; Miller, M. *Appl. Phys. Lett.* **2002**, *81*, 4607.
(12) Hikmet, R. A. M. *J. Appl. Phys.* **1990**, *68*, 4406.

10.1021/cm071727q CCC: $37.00
Published on Web 10/12/2007

monomer blends are homogeneous on deposition. Phase separation can then be induced and controlled by thermal or photoinduced polymerization in a reproducible and controllable way.[13,14] The polymer networks formed by thermally or photochemically initiated polymerization of the reactive mesogen monomers are highly cross-linked, so that the phase separated morphology is expected to be intractable and mechanically as well as thermally stable over time. Nematic calamitic LCs have mobility values, which are orders of magnitude higher, up to 10^{-2} cm^2 V^{-1} s^{-1}, than amorphous materials.[15−17] This occurs even in unaligned systems because their short range orientational order is high, giving short intermolecular separations for rapid hopping transport.[17] Low mobility is a critical factor limiting the performance of the current generation of organic photovoltaics. Reactive mesogens are compatible with ink-jet printing and roll-to-roll processing and can also be photolithographically patterned. Despite this there has been no published research on calamitic LC composites for photovoltaics except for the LC gel work discussed above,[1] although photoconductive LC composites have been studied.[19,20] An interpenetrating polymer network was formed from a homogeneous blend of an isotropic semiconducting monomer and an inert monomer by light-induced demixing.[13] Nematic LC polymer networks have been used to obtain polarized electroluminescence in photoaligned devices[21,22] and in a pixellated full color organic light emitting device.[23]

In this paper we investigate two alternatives to the LC gel approach, which are also based on liquid crystalline composites, to create a porous interface between ED and EA materials in an organic photovoltaic. In the first approach isotropic EA material is removed from a phase separated polymer network formed by cross-linking a blend of the EA material with a polymerizable nematic LC with ED properties. In the second approach a single component ED polymerizable nematic LC is partially cross-linked and washed to obtain a roughened surface. In both cases a layer of EA material is used to infill the pores and form a two-layer photovoltaic device. We discuss charge transfer between the ED and EA materials and correlate the device performance to the spatial features of the porous surface.

II. Experimental Section

Materials Synthesis. The reactive mesogen **1** exhibits a symmetrical A−B−A molecular structure and is prepared by a convergent synthesis shown in reaction Scheme 1.[24] 4-Bromophenol is converted into 1-bromo-4-octyloxybenzene in a standard Williamson ether synthesis. Reaction of this aryl bromide with 2-(tributylstannyl)thiophene in a Stille reaction[25] yields the corresponding 1-octyloxy-4-(thiophen-2-yl)benzene. This thiophene derivative is converted in turn into a 2-thiophenyltributylstannyl Stille reagent by reaction of its lithium derivative, produced by reaction with BuLi at −78 °C, with tributylstannyl chloride.[26] This tributylstannyl derivative is sensitive to acidic conditions and undergoes destannylation on contact with silica gel.[27] Fortunately the crude product is pure enough to be used to react in the next step with 2-bromo-7-iodo-9,9-dioctylfluorene prepared according to standard procedures.[28] The resultant intermediate 2-bromo-7-[2-(4-octyloxyphenyl)-thiophen-5-yl]-9,9-dihexylfluorene is converted into 2-{2-[2-(4-octyloxyphenyl)thiophen-5-yl]-9,9-dihexylfluoren-7-yl}-4,4,5,5,-tetramethyl-1,3,2-dioxaborolane by reaction with 2-isopropoxy-4,4,5,5,-tetramethyl-1,3,2-dioxaborolane at −78 °C.[29] The [2,2′]bithiophene is converted into a [2,2′]bithiophen-5-yl-tributylstannane Stille reagent by reaction of its lithium derivative, produced by reaction with BuLi at −78 °C, with tributylstannyl chloride,[26] followed by reaction with 2,7-dibromo-9,9-dioctylfluorene, produced as usual from 2,7-dibromofluorene,[30] in a Stille reaction[25] to yield 2,7-bis-[2-(thiophen-2-yl)thiophen-5-yl]-9,9-dioctylfluorene followed by selective bromination[31] in the 2-position of each thiophene to yield 2,7-bis[2-(2-bromothiophen-5-yl)thiophen-5-yl]-9,9-dioctylfluorene. The 2-{2-[2-(4-octyloxyphenyl)thiophen-5-yl]-9,9-dihexylfluoren-7-yl}-4,4,5,5,-tetramethyl-1,3,2-dioxaborolane is reacted with 2,7-bis[2-(2-bromothiophen-5-yl)thiophen-5-yl]-9,9-dioctylfluorene in a Suzuki reaction[32] to yield the octyloxy-substituted ether precursor to the desired final product **1**. The octyloxy chains are removed in a dealkylation reaction[33] with boron tribromide at 0 °C to yield the corresponding phenol, which is then alkylated in a standard Williamson ether reaction with 1,4-pentadien-3-yl 11-bromoundecanoate[34] to yield the desired compound **1**. The electron acceptor **2** was synthesized by condensation[35] of 2-amino-9,9-dioctylfluorene with commercially available perylene-3,4,9,10-tetracarboxylic dianhydride. The 2-amino-9,9-dioctylfluorene was prepared by an alkylation step in the usual way[31] from commercially available 2-aminofluorene. Experimental details are supplied for the new reaction intermediates and final products.The structures of intermediates and final products were confirmed by proton (^{1}H) nuclear magnetic resonance (NMR) spectroscopy (JOEL JMN-GX270 FT nuclear resonance spectrometer), infrared (IR) spec-

(13) Behl, M.; Zentel, R.; Broer, D. J. *Macromol. Rapid Commun.* **2004**, *25*, 1765.
(14) Ibn-Elhaj, M.; Schadt, M. *Nature* **2001**, *410*, 796.
(15) Farrar, S. R.; Contoret, A. E. A.; O'Neill, M.; Nicholls, J. E.; Richards, G. J.; Kelly, S. M. *Phys. Rev. B* **2002**, *66*, 125107.
(16) Yasuda, T.; Fujita, K.; Tsutsui, T.; Geng, Y. H.; Culligan, S. W.; Chen, S. H. *Chem. Mater.* **2005**, *17*, 264.
(17) Woon, K. L.; Aldred, M. P.; Richards, G. J.; Vlachos, P.; Mehl, G. H.; Kelly, S. M.; O'Neill, M. *Chem. Mater.* **2006**, *8*, 2311.
(18) Coakley, K. M.; McGehee, M. D. *Chem. Mater.* **2004**, *16*, 4533.
(19) Yoshimoto, N.; Hanna, J. *Adv. Mater.* **2002**, *14*, 988.
(20) Prasad, S. K.; Fair, G. G.; Hegde, G.; Hiremath, U. S.; Yelamaggad, C. V. *Liq. Cryst.* **2004**, *31*, 1265.
(21) Contoret, A. E. A.; Farrar, S. R.; Jackson, P. O.; May, L.; O'Neill, M.; Nicholls, J. E.; Richards, G. J.; Kelly, S. M. *Adv. Mater.* **2000**, *12*, 971.
(22) Aldred, M. P.; Vlachos, P.; Contoret, A. E. A.; Farrar, S. R.; Tsoi, W. C.; Hudson, R.; Woon, K. L.; Kelly, S. M.; O'Neill, M. *J. Mater. Chem.* **2005**, *15*, 3208.
(23) Aldred, M. P.; Contoret, A. E. A.; Farrar, S. R.; Kelly, S. M.; Mathieson, D.; O'Neill, M.; Tsoi, W. C.; Vlachos, P. *Adv. Mater.* **2005**, *17*, 1368.
(24) Aldred, M. P.; Contoret, A. E. A.; Devine, P. E.; Farrar, S. R.; Hudson, R.; Kelly, S. M.; Koch, G. C.; O'Neill, M.; Tsoi, W. C.; Woon, K. L.; Vlachos, P. In *Organic Thin-Film Electronics;* Arias, A. C., Tessler, N., Burgi, L., Emerson, J. A., Eds.; Mater. Res. Soc. Symp. Proc. 871E, Warrendale, PA , 2005; p I10.7.
(25) Stille, J. K. *Angew. Chem., Int. Ed. Eng.* **1986**, *25*, 508.
(26) Vlachos, P. Ph.D. Thesis, University of Hull, 2003.
(27) Miller, L. L.; Yu, Y. *J. Org. Chem.* **1995**, *60*, 6813.
(28) Khan, S. M.; Al-Mandhary, M. R. A.; Al-Suti, M. K.; Ahrens, B.; Mahon, M. F.; Male, L.; Raithby, P. R.; Boothby, C. E.; Koehler, A. *Dalton Trans.* **2003**, 74.
(29) Günter, R.; Farrell, T.; Scherf, U.; Miteva, T.; Yasuda, A.; Nelles, G. *J. Mater. Chem.* **2004**, *14*, 2622.
(30) Kelley, C. J.; Ghiorghis, A.; Kauffman, J. M. *J. Chem. Res. (M)* **1997**, 2710.
(31) Ramanathan, V.; Levine, R. *J. Org. Chem.* **1962**, *27*, 121.
(32) Suzuki, A. *Pure. Appl. Chem.* **1994**, *66*, 213.
(33) McOmie, J. F.; Watts, M. L.; West, D. E. *Tetrahedron* **1968**, *24*, 2289.
(34) Aldred, M. P.; Eastwood, A. J.; Kelly, S. M.; Vlachos, P.; Mansoor, B.; O'Neill, M.; Tsoi, W. C. *Chem. Mater.* **2004**, *16*, 4928.
(35) Langhals, H.; Sprenger, S.; Brandherm, M.-T. *Liebigs Ann.* **1996**, *10*, 1587.

Scheme 1[a]

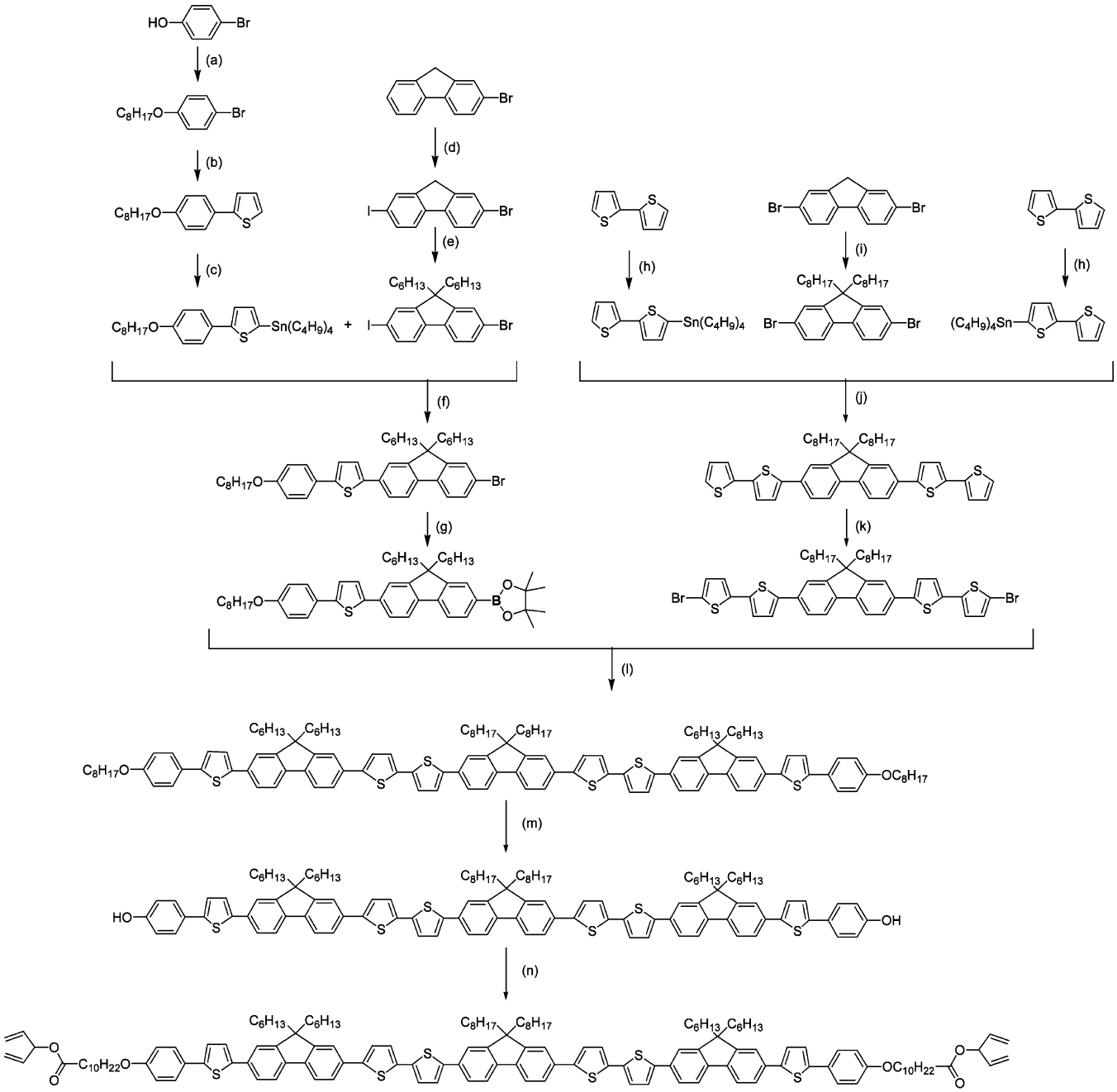

compound **1**

[a] Reagents: (a) K_2CO_3, KI, butanone, $C_8H_{17}Br$ (reflux); (b) $Pd(PPh_3)_4$, DMF (80 °C); (c) *n*-butyllithium, $Sn(C_4H_9)_3Cl$, THF (−78 °C); (d) AcOH, H_2SO_4, H_2O, H_5IO_6, I_2 (80 °C); (e) NaOH, TBAB, toluene, $C_8H_{17}Br$ (reflux); (f) $Pd(PPh_3)_4$, DMF (80 °C); (g) *n*-butyllithium, $C_8H_{17}BO_3$, THF (−78 °C); (h) *n*-butyllithium, $Sn(C_4H_9)_3Cl$, THF (−78 °C); (i) NaOH, TBAB, toluene, $C_6H_{13}Br$ (reflux); (j) $Pd(PPh_3)_4$, DMF (80 °C); (k) *N*-bromosuccinimide, CH_3CO_2H, CH_2Cl_2; (l) $Pd(PPh_3)_4$, K_3PO_4, DMF (80 °C); (m) (i) BBr_3, CH_2Cl_2 (0 °C); (ii) H_2O; (n) K_2CO_3, KI, DMF (80 °C).

troscopy (Perkin-Elmer 783 infrared spectrophotometer), and mass spectrometry (MS) (Finnegan MAT 1020 automated GC/MS). Reaction progress and product purity were checked using a CHROMPACK CP 9001 capillary gas chromatograph fitted with a 10 m CP-SIL 5CB (0.12 μm, 0.25 mm) capillary column. All of the final products were more than 99.5% pure by GLC. Transition temperatures were determined using an Olympus BH-2 polarizing light microscope together with a Mettler FP52 heating stage and a Mettler FP5 temperature control unit. The analysis of transition temperatures and enthalpies was carried out by a Perkin-Elmer DSC7-PC differential scanning calorimeter. The octyloxy chain was used as a protecting group during the synthesis of compound **1** as the starting material for Scheme 1 was available from another program and longer chains are easier to remove than shorter ones. We now usually use branched alkoxy chains, such as citronenyloxy groups, since they act as a better protecting group in terms of lowering the melting point of the reaction intermediates and increasing their solubility in organic solvents.

2-{2-[2-(4-Octyloxyphenyl)thiophen-5-yl]-9,9-dihexylfluoren-7-yl}-4,4,5,5-tetramethyl-1,3,2-dioxaborolane. Butyllithium (8.20 cm^3 of 2.5 M in hexanes, 0.020 mol) was added dropwise to a stirred solution of 2-(2-bromo-9,9-dioctylfluoren-7-yl)-5-(4-

Scheme 2[a]

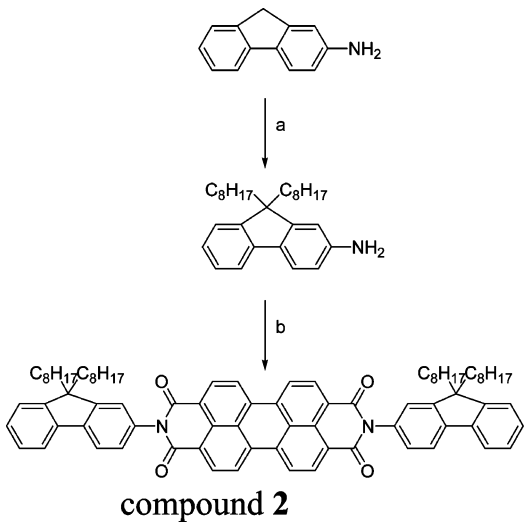

[a] Reagents: (a) KOH, KI, $C_8H_{17}Br$, DMSO; (b) perylene-3,4,9,10-tetracarboxylic dianhydride, $Zn(OAc)_2{\cdot}2H_2O$, imadazole.

octyloxyphenyl)thiophene (12.00 g, 0.0170 mol) in THF (200 cm^3) at −78 °C. The reaction mixture was stirred at −78 °C for 2 h, and then 2-isopropoxy-4,4,5,5-tetramethyl-1,3,2-dioxoborolane (4.80 g, 0.0250 mol) was added dropwise while a temperature of −78 °C was maintained. On complete addition the temperature was allowed to slowly warm to room temperature, and the solution was stirred overnight. The reaction mixture was poured into water (300 cm^3), and the crude product was extracted into diethyl ether (3 × 200 cm^3). The combined organic extracts were washed with water (2 × 200 cm^3), dried ($MgSO_4$), filtered, and concentrated under reduced pressure. Purification was carried out by flash chromatography [silica gel; DCM/hexane 3:17 increasing to DCM/hexane 1:3] to yield 10.20 g (80%) of a pale yellow oil, which was used in the next step without further purification.

2,7-Bis[2-(thiophen-2-yl)thiophen-5-yl]-9,9-dioctylfluorene. Tetrakis(triphenylphosphine)palladium(0) (1.48 g, 0.00128 mol) was added to a stirred degassed solution of [2,2′]bithiophenyl-5-yl-tributylstannane (16.38 g, 0.0360 mol), 2,7-dibromo-9,9-dioctylfluorene (7.00 g, 0.0128 mol). and DMF (100 cm^3) at room temperature. The reaction mixture was heated under reflux for 24 h. The cooled reaction mixture was added to water (100 cm^3), and the product was extracted into DCM (3 × 100 cm^3). The combined organic extracts were washed with a saturated potassium fluoride solution (2 × 200 cm^3) and water (3 × 100 cm^3), dried ($MgSO_4$), filtered, and concentrated under reduced pressure. The crude product was purified by column chromatography [silica gel; DCM/hexane 3:17] and recrystallization from DCM/EtOH to yield 4.00 g (47%) of a yellow crystalline solid. Melting point: 144−146 °C. ^{1}H NMR ($CDCl_3$) δ_H: 0.69 (4H, quint), 0.79 (3H, t, J = 6.8 Hz), 1.07−1.21 (20H, m), 2.00−2.04 (4H, m), 7.05 (2H, dd, J = 4.9, 3.7 Hz), 7.18 (2H, d, J = 3.7 Hz), 7.22−7.26 (4H, m), 7.30 (2H, d, J = 3.8 Hz), 7.54 (2H, d, J = 1.3 Hz), 7.60 (2H, dd, J = 7.9, 1.6 Hz), 7.68 (2H, d, J = 7.9 Hz). IR ν_{max}/cm^{-1}: 2956, 2924, 2851, 1605, 1474, 1425, 1376, 1076, 840, 819, 794, 688. MS-EI/+ve ion: 720, 719, 718 (M^+, M100).

2,7-Bis[2-(2-bromothiophen-5-yl)thiophen-5-yl]-9,9-dioctylfluorene. *N*-Bromosuccinamide (1.98 g, 0.011 mol) was added in small portions over 2 h to a solution of 2,7-bis[2-(thiophen-2-yl)thiophen-5-yl]-9,9-dioctylfluorene (4.00 g, 5.56 × 10^{-3} mol) in AcOH (50 cm^3) and DCM (50 cm^3). The reaction progress was monitored by TLC, and once completed the solution was poured into a 20% aqueous sodium metabisulfite solution (300 cm^3). The crude product was extracted into DCM (3 × 100 cm^3), and the combined organic extracts were washed with water (3 × 200 cm^3), dried ($MgSO_4$), filtered, and concentrated under reduced pressure. The crude product was purified by column chromatography [silica gel; DCM/hexane 1:4] and recrystallization from DCM/EtOH to yield 4.00 g (83%) of a yellow crystalline solid. Melting point: 153−154 °C. ^{1}H NMR ($CDCl_3$) δ_H: 0.68 (4H, quint), 0.79 (3H, t, J = 7 Hz), 1.06−1.20 (20H, m), 2.00−2.04 (4H, m), 6.96 (2H, d, J = 3.8 Hz), 7.00 (2H, d, J = 3.8 Hz), 7.11 (2H, d, J = 3.6 Hz), 7.28 (2H, d, J = 3.8 Hz), 7.53 (2H, d, J = 1.1 Hz), 7.58 (2H, dd, J = 7.9, 1.7 Hz), 7.68 (2H, d, J = 7.5 Hz). IR ν_{max}/cm^{-1}: 2954, 2923, 2851, 1605, 1514, 1474, 1422, 1376, 1258, 1067, 970, 872, 816, 788. MS-MALDI/+ve ion: 879, 878, 877, 876 (M^+).

Tetrakis(triphenylphosphine)palladium(0) (0.30 g, 2.60 × 10^{-4} mol) was added to a stirred degassed solution of 2-{2-[2-(4-octyloxyphenyl)thiophen-5-yl]-9,9-dihexylfluoren-7-yl}-4,4,5,5-tetramethyl-1,3,2-dioxaborolane (4.20 g, 5.67 × 10^{-3} mol), bis[2-(2-bromothiophen-5-yl)thiophen-5-yl]-9,9-dioctylfluorene (2.00 g, 2.27 × 10^{-3} mol), tripotassium phosphate (1.44 g, 6.78 × 10^{-3} mol), and DMF (100 cm^3). The mixture was heated (80 °C) and stirred overnight. The cooled reaction mixture was poured into water, and the crude product was extracted into diethyl ether (3 × 150 cm^3). The combined organic extracts were washed with brine (2 × 200 cm^3), dried ($MgSO_4$), filtered, and concentrated under reduced pressure. The crude product was purified by column chromatography [silica gel, DCM/hexane 1:1] and recrystallized from DCM/EtOH to yield 3.20 g (72%) of an orange crystalline solid. Transition temperature, T_g = 46 °C; Cr−N = 55 °C; N−I = 235 °C. ^{1}H NMR ($CDCl_3$) δ_H: 0.66−0.81 (30H, m), 0.90 (6H, t, J = 6.7 Hz), 1.07−1.19 (34H, m), 1.27−1.38 (16H, m), 1.48 (4H, quint), 1.80 (4H, quint), 2.01−2.06 (12H, m), 4.00 (4H, t, J = 6.7 Hz), 6.93 (4H, d, J = 8.7 Hz), 7.21 (2H, d, J = 3.9 Hz), 7.24 (4H, d, J = 3.9 Hz), 7.33−7.35 (6H, m), 7.57−7.63 (16H, m), 7.68−7.70 (6H, m). IR ν_{max}/cm^{-1}: 3455, 2924, 2876, 1604, 1467, 1247, 1105, 1005, 791. MS-MALDI/+ve ion: 1958, 1957, 1956, 1955 (M^+).

2,7-Bis[2-(2-{2-[2-(4-hydroxyphenyl)thiophen-5-yl]-9,9-dihexylfluoren-7-yl}thiophen-5-yl)thiophen-5-yl]-9,9-dioctylfluorene. Boron tribromide (0.95 g, 3.83 × 10^{-3} mol) was added dropwise to a cooled solution, 0 °C, of 2,7-bis[2-(2-{2-[2-(4-octyloxyphenyl)-thiophen-5-yl]-9,9-dihexylfluoren-7-yl}thiophen-5-yl)thiophen-5-yl]-9,9-dioctylfluorene (2.50 g, 1.27 × 10^{-3} mol) in DCM (150 cm^3). The mixture was allowed to warm to room temperature and was stirred overnight. The mixture was poured onto an ice/water mixture (300 cm^3) and stirred for 1 h. The crude product was extracted into ethyl acetate (4 × 100 cm^3), and the combined organic extracts were washed with water (2 × 200 cm^3), dried ($MgSO_4$), filtered, and concentrated under reduced pressure. The crude product was purified by flash chromatography [silica gel; ethyl acetate/hexane 1:4 increasing to ethyl acetate/hexane 2:3] to yield 1.70 g (77%) of an orange crystalline solid. T_g = 86 °C; N−I = 233 °C. ^{1}H NMR ($CDCl_3$) d_H: 0.66−0.81 (30H, m), 1.1−1.19 (34H, m), 2.0−2.08 (12H, m), 4.90 (2H, s), 6.88 (2H, d, J = 8.8 Hz), 7.21 (2H, d, J = 3.6 Hz), 7.24 (4H, d, J = 3.6 Hz), 7.33−7.35 (6H, m), 7.54−7.57 (10H, m), 7.62 (6H, dd, J = 7.8, 1.6 Hz), 7.68−7.71 (6H, m). IR ν_{max}/cm^{-1}: 3412, 2924, 2853, 1703, 1608, 1511, 1469, 1360, 1172, 1088, 795. MS-MALDI/+ve ion: 1736, 1735, 1734, 1733, 1732 (M^+), 1731.

Compound 1. A mixture of 2,7-bis[2-(2-{2-[2-(4-hydroxyphenyl)thiophen-5-yl]-9,9-dihexylfluoren-7-yl}thiophen-5-yl)thiophen-5-yl]-9,9-dioctylfluorene (1.00 g, 5.77 × 10^{-4} mol), anhydrous potassium carbonate (0.23 g, 1.73 × 10^{-3} mol), potassium iodide (0.10 g, 5.77 × 10^{-5} mol), and DMF (50 cm^3) was heated (80 °C) and stirred overnight. 1,4-Pentadien-3-yl 11-bromoundecanoate (0.57 g, 1.72 × 10^{-3} mol) was added to the reaction mixture, the

reaction temperature was maintained, and the mixture was stirred for a further 24 h. The cooled mixture was poured into water (200 cm^3), and the crude product was extracted into diethyl ether (3 × 100 cm^3). The combined organic extracts were washed with brine (2 × 100 cm^3), dried ($MgSO_4$), filtered, and concentrated under reduced pressure. The crude product was purified by column chromatography [silica gel, DCM/hexane 1:1] and recrystallized from DCM/EtOH to yield 0.81 g (63%) of an orange crystalline solid. T_g = 26 °C; N−I = 188 °C. ^{1}H NMR ($CDCl_3$) δ_H: 0.71−0.82 (24H, m), 1.03−1.19 (44H m), 1.31−1.39 (20H, m), 1.47 (4H, quint), 1.65 (4H, quint), 1.80 (4H, quint), 1.99−2.08 (12H, m), 2.35 (4H, t, J = 7.3 Hz), 4.00 (4H, t, J = 6.4 Hz), 5.22−5.32 (8H, m), 5.72−5.73 (2H, m), 5.80−5.88 (4H, m), 6.93 (4H, d, J = 8.7 Hz), 7.22 (2H, d, J = 3.6 Hz), 7.24 (4H, d, J = 3.9 Hz), 7.34−7.35 (6H, m), 7.58 (10H, d, J = 8.4 Hz), 7.62 (6H, d, J = 7 Hz), 7.68−7.71 (6H, m). IR ν_{max}/cm^{-1}: 3081, 2955, 2930, 2870, 1736, 1610, 1570, 1511, 1474, 1280, 1256, 1179, 1165, 1113, 1070, 840, 799. MS-MALDI/+ve ion: 2233, 2232 (M^+), 2231.

9,9-Dioctylfluoren-2-ylamine. Powdered potassium hydroxide (6.58 g, 0.1173 mol) was added in small portions to a solution of 2-aminofluorene (5.00 g, 0.0276 mol), 1-bromooctane (11.72 g, 0.0607 mol), potassium iodide (0.46 g, 0.0028 mol), and DMSO (100 cm^3). The mixture was stirred at room temperature for 2 h and then poured into water (300 cm^3). The crude product was extracted into diethyl ether (4 × 150 cm^3), and the combined organic extracts were washed with water (100 cm^3), HCl (aqueous) (100 cm^3, 20% v/v), and brine (2 × 250 cm^3). Purification was carried out by column chromatography [silica gel, ethyl acetate/hexane 1:5] to yield 8.94 g (80%) of a pale yellow crystalline solid. Melting point: 77−78 °C. ^{1}H NMR ($CDCl_3$) δ_H: 0.61 (4H, quint), 0.81 (6H, t, J = 7.3 Hz), 1.03−1.20 (20H, m), 1.89 (4H, m), 6.77 (2H, d, J = 7.8 Hz), 7.19−7.28 (3H, m), 7.50 (1H, dd, J = 7.6, 0.8 Hz), 7.55 (1H, d, J = 8.4 Hz). IR ν_{max}/cm^{-1}: 3453, 3366, 3004, 2954, 2924, 2848, 1622, 1582, 1494, 1454, 1352, 1327, 1275, 1256, 1211, 1134, 1024, 864, 820, 773, 738, 588, 562. MS-EI/+ve ion: 407, 406, 405 (M^+).

Compound 2. A mixture of 2-amino-9,9-dioctylfluorene (3.10 g, 0.0076 mol), perylene-3,4,9,10-tetracarboxylic dianhydride (1.00 g, 0.0025 mol), zinc acetate dihydrate (0.28 g, 0.0013 mol), and imidazole (10.00 g) was heated (120 °C) and stirred overnight. Hydrochloric acid (aqueous) (200 cm^3, 20% v/v) was added to the cooled mixture, and the crude product was extracted into DCM (4 × 100 cm^3). The combined organic extracts were washed with water (2 × 200 cm^3), dried ($MgSO_4$), filtered, and concentrated under reduced pressure. Purification was carried out by column chromatography [silica gel, DCM] and recrystallized from EtOH/DCM to yield 1.56 g (52%) of a dark red crystalline solid. Melting point: 274 °C. ^{1}H NMR ($CDCl_3$) δ_H: 0.66−0.78 (8H, m), 0.86 (12H, t, J = 6.4 Hz), 1.09−1.27 (40H, m), 1.99 (8H, t, J = 8.3 Hz), 7.31−7.39 (10H, m), 7.76 (2H, dd, J = 7.2, 1.7 Hz), 7.88 (2H, d, J = 8.7 Hz), 8.72 (4H, d, J = 8.2 Hz), 8.79 (4H, d, J = 7.9 Hz). IR ν_{max}/cm^{-1}: 3500, 2926, 2852, 17−4, 1660, 1583, 1577, 1453, 1403, 1356, 1253, 1177, 969, 810, 745. MS-MALDI/+ve ion: 1169, 1168, 1167 (M^+). Elemental analysis: expected: C 84.35%, H 7.77%, N 2.40%; obtained: C 84.09%, H 8.00%, N 2.10%.

Analytical Methods. The thermotropic mesophases observed for compound **1** were investigated using differential scanning calorimetry (DSC) and optical microscopy between crossed polarizers. DSC was also used to obtain the glass transition temperature, T_g. The ionization potential (IP) of compound **1** and the electron affinity (EA) of compound **2** were measured electrochemically by cyclic voltammetry using a computer-controlled scanning potentiostat (Solartron 1285) as described elsewhere.[35] The photoinduced absorption (PIA) experiment was carried out using a standard pump−probe setup. A GaN laser of wavelength 405 nm was used as the pump source, and a tungsten-halogen lamp was used as the probe. A monochromator was used to disperse the probe light, and a silicon and indium gallium arsenide photodiode was used to detect light of energy > and < 1.24 eV, respectively. A dual phase lock-in amplifier was used to measure $\Delta T/T$. A Picoscan scanning probe microscope from Molecular Imaging was used to obtain the digitized atomic force microscopy (AFM) scans. The amplitude of the surface roughness is defined as $|z_{kl}|$, the modulus of the deviation of the surface amplitude from a mean value, where k and l are the pixel numbers in the x and y directions. The roughness distribution is obtained from the number of samples having a given roughness amplitude. The power spectral density (PSD) is given as

$$\mathrm{PSD}(n,m) = \left| \frac{1}{N_k N_l} \sum_{k=0}^{N_k-1} \sum_{l=0}^{N_l-1} z_{kl} e^{-2\pi j[(nk/N_k)+(ml/N_l)]} \right|^2, \quad n = 0 \ldots N_k - 1,\ m = 0 \ldots N_l - 1$$

where N_k and N_l are the total number of pixels in the x and y directions, respectively. The photovoltaic devices were fabricated on indium tin oxide coated glass (13Ω $^{-1}$) coated with a polystyrene sulfonate/polyethylene dioxythiophene (PSS/PEDOT, Baytron P VP CH 8000, Bayer). The PSS/PEDOT layer was baked at 150 °C for 10 min. Device A was prepared by spin casting at 2000 rpm for 30 s from a solution of **1** and **2** in toluene (20 mg mL^{-1}) in the ratio 7:3 by weight. The film was heated at 70 °C for 20 min and cross-linked at room temperature using a HeCd laser of wavelength 325 nm and fluence 1100 J cm^{-2}. The film was then washed by spinning in toluene, and then the solvent was evaporated as described before. The layer thickness was ≈50 nm. The active layer of device C was prepared similarly but was not washed. The active layer of device B was processed similarly from a solution of **1** in toluene (20 mg mL^{-1}). A fluence of 500 J cm^{-2} was used to partially cross-link the layer, and the film thickness was ≈120 nm after washing. Device A and B were coated with a 60 nm layer of **2**, deposited by spin-casting and baked at 120 °C. Device C had no overlying organic layer. The three devices had cathodes of lithium fluoride (1 nm) and aluminum. The current−voltage characteristics of the photovoltaic devices were measured using a Visual-Basic controlled picoammeter in the dark and on illumination with a Xenon lamp dispersed through a monochromator.

III. Results and Discussion

Mesophase Identification. Compound **1** is a polymerizable liquid crystal, with the transition temperatures T_g = 26 °C; N−I = 188 °C. The only phase observed is the nematic phase. Bright nematic droplets were observed using polarizing optical microscopy on cooling from the black isotropic liquid to form the Schlieren texture with two- and four-point brushes characteristic of the nematic phase along with some optically extinct homeotropic areas. As the sample was cooled further the texture often formed more optically extinct homeotropic areas, which indicates that the phase is indeed optically uniaxial. The birefringent and homeotropic areas flashed brightly under any mechanical disturbance. This behavior and the simultaneous presence of both the homeotropic texture and the Schlieren texture confirms that the mesophase observed is indeed a nematic phase. On further cooling to room temperature, compound **1** does not crystallize but remains in a nematic glassy state. The transition temperature was confirmed by DSC to within 1−2 °C. Compound **2** is a crystalline solid with a high melting point

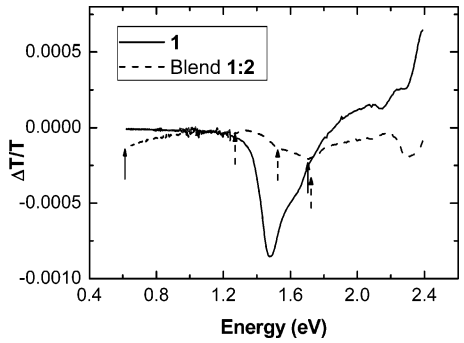

Figure 1. Spectral dependence of the photoinduced change of transmission of a thin film of **1** and a blended film of **1:2** on excitation with a GaN laser at 405 nm. The positive and negative polaron transitions are labeled with solid and dashed arrows, respectively.

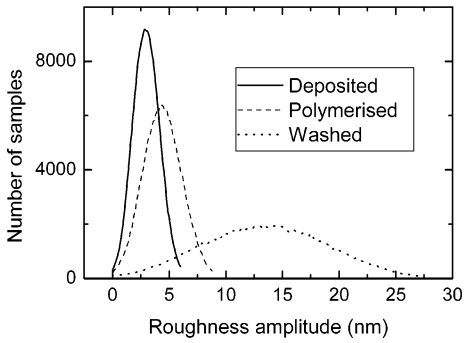

Figure 2. Distribution of the amplitude of surface roughness for a blend of **1:2**.

of 274 °C. It has a large molecular core, which may result in a highly viscous isotropic melt. This may explain the formation of a long-lived metastable glassy state on rapid cooling a thin film from the isotropic liquid. A blend of **1** and **2** in the ratio of 7:3 by weight is also a liquid crystal glass with a glass transition temperature of 21 °C and a clearing point (N−I) of 132 °C. This also supercools so that the blend remains in the nematic glassy state at room temperature for many weeks.

Charge Separation. Compound **1** was chosen as the electron-donating species for the photovoltaic device because of its complementary absorption spectrum (from 340 to 525 nm) to that of compound **2** (420−600 nm). Compound **1** also has a relatively high hole mobility of 1.6×10^{-3} cm^2 V^{-1} s^{-1} as measured by time-of-flight at room temperature. This compares with a value of 2×10^{-5} cm^2 V^{-1} s^{-1} for the electron-donating reactive mesogen used in our original photovoltaic device.[15] Compound **1** has a low IP of 5.25 eV, so that it is suitable for use as the electron-donating species in the blend. **2** has a high EA of 3.94 eV, measured by cyclic voltammetry, which confirms its suitability to form the electron-accepting layer of the device. The difference between the IP of **1** and the EA of **2** is 1.31 eV. This is smaller than the energy of the absorption band-edge of both materials, equal to 2.38 and 2.13 eV for **1** and **2**, respectively, so that charge separation at the donor−acceptor interface is thermodynamically favorable. This analysis assumes that no charge transfer occurs between **1** and **2** so more direct evidence of charge separation is required.

The PIA of a blend of **1** and **2** was studied to experimentally check for charge transfer. Figure 1 shows the wavelength dependence of the photoinduced change in transmission ($\Delta T/T$) for a sample of **1** and a blend of **1** and **2** in the ratio 1:1 by weight at 80 K. A thin film of **2** shows no PIA signal because of negligible absorption at the pump wavelength of 405 nm. In the pristine sample of **1**, the PIA is dominated by a triplet transition with a peak at 1.48 eV and a vibronic sideband at 1.64 eV.[36] There is also a positive photobleaching signal above 1.87 eV originating from saturation of the S_0-S_1 transition.[37] In the blend the triplet signal is quenched, and the broad PIA signal has three peaks at 1.70, 1.52, and 1.27 eV (dashed arrows in Figure 3), which may be attributed to the absorption of the negative polaron of **2** by comparison with the PIA of the negative polaron of perylene in a conjugated oligo(p-phenylene vinylene) with dangling perylene bisimides.[38] The reported spectrum has 3 peaks at 1.28 eV, 1.54 eV, and 1.72 eV, which agrees very well with the spectrum presented here. These peaks are also observed in blends of **2** with other electron-donating materials confirming their association with **2**.[39] The low-energy signal below 1.0 eV in Figure 2 is assigned to the P1 transition of the positive polaron of **1** because of its long dispersive lifetime and by comparison with similar transitions in polyfluorene related compounds.[40,41] A comparison with spectra from chemically doped samples suggests that the high-energy P2 transition of the polaron lies between 1.61 and 1.78 eV, so overlapping the high-energy negative polaron transition.[36,38] The blend transition at 2.4 eV is an artifact observed in many unrelated spectra. The quenching of the triplet and the observation of polarons in the PIA spectrum of the blend confirms charge separation of the blend, The photoluminescence quantum efficiency of **1** is 35% at room temperature. This PL is quenched by a factor of 400 in the blend as a final indication of charge separation.

Formation and Analysis of Distributed Interface. We now examine the formation of a LC polymer network composite with a porous surface for use as the lower ED layer of a bilayer photovoltaic device. Two distinct approaches are adopted. First a homogeneous liquid crystalline blend of 1:2 is deposited by spin casting. It is well-known that the miscibility of the components of a blend changes when one component is polymerized,[42] so that the two materials phase separate on exposure to ultraviolet light. Figure 2 shows the distribution of the surface roughness amplitude of the film, obtained from digitized AFM images, following deposition and then polymerization and after washing in toluene to remove the unpolymerized material from the surface. The peak of the distribution increases from 2.8 to 4.4 nm as a result of photoinduced roughness during

(36) Tsoi, W. C.; O'Neill, M.; Aldred, M. P.; Vlachos, P.; Kelly, S. M. *J. Chem. Phys.* **2007**, *127*, 114901.
(37) Dellepiane, G.; Cuniberti, C.; Comoretto, D.; Musso, G. F.; and Figari, G. *Phys. Rev. B* **1993**, *48*, 7850.
(38) Neuteboom, E. E.; van Hal, P. A.; Janssen, R. A. J. *Chem. Eur. J.* **2004**, *10*, 3907.
(39) Tsoi, W. C. Ph.D. Thesis, University of Hull, 2006.
(40) Cadby, A. J.; Lane, P. A.; Mellor, H.; Martin, S. J.; Grell, M.; Giebeler, C.; Bradley, D. D. C.; Wohlgenannt, M.; Vardeny, Z. V. *Phys. Rev. B*: *Condens. Matter Mater. Phys.* **2000**, *62*, 15604.
(41) Pogantsch, A.; Wenzl, F. P.; Scherf, U.; Grimsdale, A. C.; Müllen, K.; List, E. J. W. *J. Chem. Phys.* **2003**, *119*, 6904.
(42) Sangermano, M. *Prog. Org. Coat.* **2006**, *55*, 225.

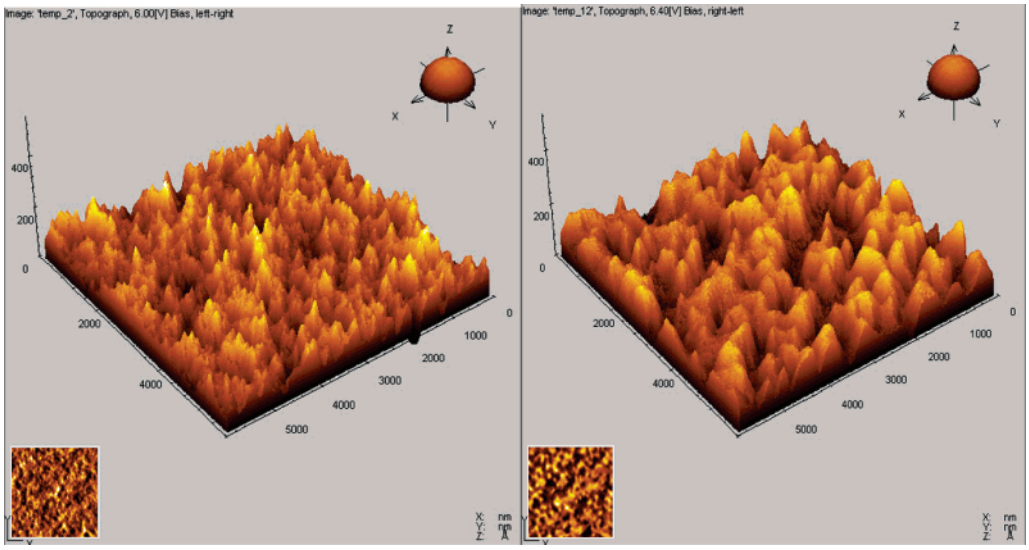

Figure 3. Left: Topographic image of the network obtained on washing a photopolymerized blend of **1:2**. Right: Topographic image of the network obtained on washing a partially photopolymerized film of **1**. Both images show an area of 6 × 6 μm^2.

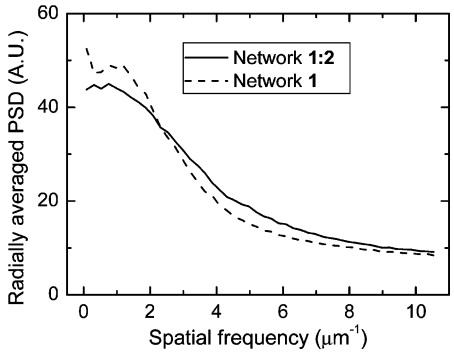

Figure 4. Power spectral density as a function of in-plane spatial frequency of the AFM images of the two networks.

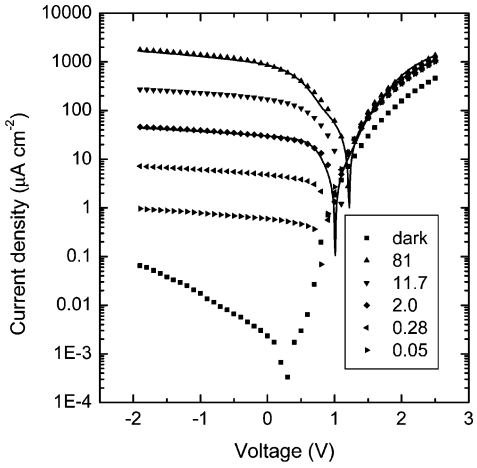

Figure 5. The current density versus voltage of the photovoltaic device A incorporating a thin film of **2** infilling the network **1:2**. The inset labels the irradiance in mW cm^{-2} of the input light source of wavelength 475 nm. The solid lines show the simulated plots using the equivalent circuit illustrated in Figure 8 for input irradiances of 81 mW cm^{-2} and 2 mW cm^{-2}.

photopolymerization. The origin of this photoinduced roughness is being investigated. The surface roughness of the polymerized sample represents the roughness of the interface of a bilayer device without the porous surface, caused by washing the film in toluene to remove some of the unpolymerized material from the surface. This process gives a significantly rougher surface with an amplitude distribution peaking at 13.3 nm and extending from 7 to 19.5 nm (fwhm). The thickness of the film is ≈50 nm so that the porous surface penetrates almost half of the layer.

Figure 3 shows an AFM image of area 6 × 6 μm^2 of the surface of the washed network. It also shows an image of a second template, which was prepared by partial polymerization and washing of a thin film of **1**, to remove the unpolymerized regions of the surface. The distribution of the roughness amplitude of the latter network is centered at 12.1 nm with a fwhm of 17.8 nm. A comparison of both images in Figure 3 suggests that the surface roughness of the **1:2** network has finer in-plane spatial features compared with the network formed from partially polymerized **1**. A PSD analysis was undertaken to quantitatively compare the in-plane spatial features of the two networks.[43] Figure 4 confirms the features expected from inspection of the images. The **1:2** network has a higher PSD than the partially polymerized network at spatial frequencies above 2.3 μm^{-1}, i.e. its surface roughness occurs on a finer in-plane spatial scale.

Photovoltaic Results and analysis. The network template provides the bottom section of the distributed interface for charge transfer in a photovoltaic device. A layer of **2** was spin-cast onto the template to infill the grooves and to provide the electron-accepting component of the interface. It also acts to planarize the surface and has an rms surface roughness of 0.6 nm. Figure 5 shows the current voltage characteristics of organic photovoltaic device A, which contains the network **1:2** with an overlying layer of **2**, in the dark and on illumination with monochromatic light of wavelength 475 nm, which gives maximum photocurrent.

Figure 5 shows the expected features of an organic photovoltaic device. The current increases with the input irradiance. The open-circuit voltage, V_{oc}, also changes with input irradiance to a saturated value of 1.2 V. This approaches the maximum value equal to 1.31 V obtainable for

(43) Vishwakarma, P. N.; Prasad, V.; Subramanyam, S. V.; Ganesan, V. *Bull. Mater. Sci.* **2005**, *28*, 609.

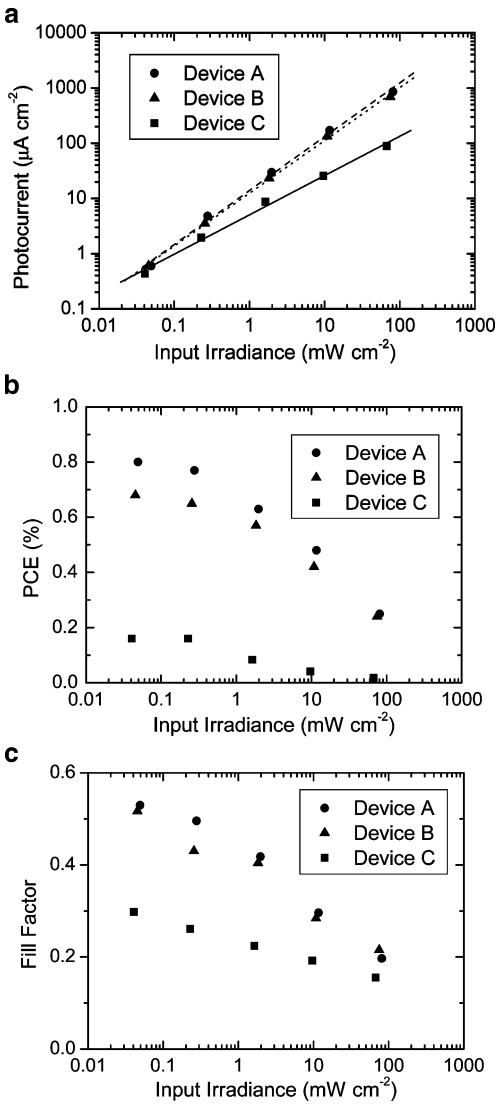

Figure 6. a. Current density (J) as a function of input irradiance (I_{in}) for the three devices. The points are experimental data, and the lines are the best fits using the function $J = AI_{in}^{b}$, where A and b are fitting parameters. b. PCE as a function of input irradiance for the three devices. c. Fill factor as a function of input irradiance for the three devices.

the material combination used. The power conversion efficiency (PCE) and external quantum efficiency (EQE) have maximum values of 0.8% and 4.5%, respectively, when the input irradiance is 0.28 mW cm^{-2}. At the highest irradiance of 81 mW cm^{-2} the PCE and EQE are 0.25% and 2.8%, respectively.

We compare the performance of three devices. Device A is described above. Device B contains a layer of **2** overlying the network formed from partially polymerized **1**. Device C contains a photopolymerized blend of **1:2** in the ratio 7:3 by weight. It has no overlying organic layer. The network used to template the distributed interface of device A is formed from the blend of **1:2**. Some of the electron-accepting **2** may remain trapped in the electron-donating polymer network of **1** forming a bulk heterojunction similar to a blend. Hence we must ascertain that the device performance results from charge separation at the vertically distributed interface between the network and the overlying layer **2** rather than the bulk heterojunction in the lower layer. Figure 6a−c shows the output current density (J), PCE, and fill factor as a function of input irradiance (I_{in}) for the three devices. The data in Figure 6a show the relationship $J = AI_{in}^{b}$, where A and b are constants. $b = 1$ implies monomolecular recombination, whereas the recombination of nongeminate electrons and holes is bimolecular with $b = 0.5$. $b = 0.98$, 0.96, and 0.71 for devices A, B, and C respectively, showing that recombination is primarily monomolecular in both bilayer porous network devices, whereas nongeminate recombination is a major limitation of device efficiency for the blend device C at high irradiances. Hence we can confirm that any bulk heterojunction in the lower layer of the porous network has a minor effect on the performance of device A.

The main motivation of this work is to explore the LC interpenetrating network concept. Of particular interest is how the spatial features of the porous interface between the electron-donating and electron-accepting layers affects the performance of the device. This can be done by comparing devices A and B. We have shown in Figure 4 that the **1:2** network used in device A has finer in-plane surface features than the template formed from partially polymerized **1** used in device B. The mean roughness amplitude is similar for both cases. This means that more photogenerated excitons should reach the interface before recombination in device A resulting in better device performance. This is indeed the case. As Figure 6a−c shows, both devices show similar trends of performance with device A having significantly higher values of J and PCE for all values of input irradiance. For example, the PCE of devices A and B is 0.63% and 0.57% for an I_{in} value of ≈2 mW cm^{-2} (measurements were taken at slightly different values of I_{in}), with a corresponding EQE of 3.9% and 3.3%, respectively. When I_{in} = ≈80 mW cm^{-2}, the corresponding PCE values are 0.25% and 0.24%, while the corresponding EQE values are 2.8% and 2.4%, respectively. This suggests that finer surface features improve device performance supporting the validity of our concept.

The maximum monochromatic PCE and EQE of device A are 0.8% and 4.5%, respectively, which is far from state of the art. These values are limited by the low photocurrent for all irradiances. Photoinduced absorption and PL quenching, as discussed above, show that exciton dissociation is virtually complete in a blend of **1** and **2**. However, as shown in Figures 2 and 4, the porous interface of device A is far from ideal: the surface roughness penetrates less than half of the layer thickness, and the in-plane spatial frequencies should extend to 50 μm^{-1} to guarantee that all excitons reach the porous interface between **1** and **2** before recombination, assuming that the exciton diffusion length is 100 Å. We plan to measure the extent of recombination before dissociation by obtaining the external quantum efficiency of PL from the devices, in comparison with a single film of **1**. Another issue limiting the performance of photovoltaic devices is the recombination of the dissociated electrons and holes. We have shown in Figure 6a that nongeminate electron−hole recombination is not a limitation for device A because the photocurrent scales almost linearly with I_{in}. However, as discussed by Mihailetchi et al.,[44] the monomolecular recombination of the bound geminate electron−hole pair can

(44) Mihailetchi, V. D.; Koster, L. J. A.; Hummelen, J. C.; Blom, P. W. M. *Phys. Rev. Lett.* **2004**, *93*, 216601.

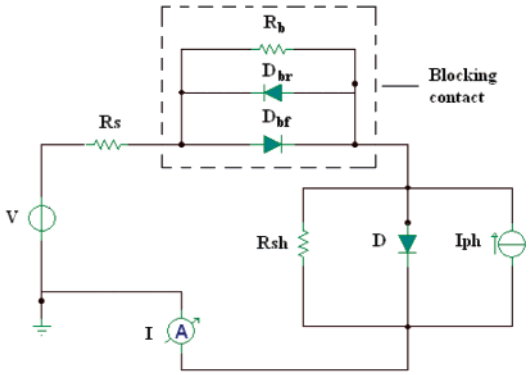

Figure 7. Equivalent circuit used to simulate the photocurrent voltage characteristics of device A. The labeled components are explained in the text.

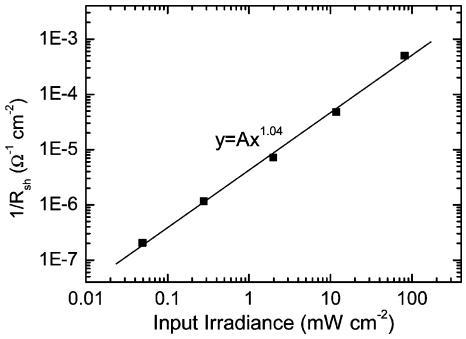

Figure 8. $1/R_{sh}$ as a function of input irradiance for device A. The data points are from experiment, and the solid line is a fit to the equation shown.

significantly limit performance. Temperature-dependent current−voltage data are required to quantify this effect.

As Figure 6b,c shows, the performance of device A, in particular the PCE and FF, deteriorates with increasing irradiance. We use an equivalent circuit, shown schematically in Figure 7, to explore the reasons for this. The current−voltage characteristics were simulated by changing the parameters of the equivalent circuit until a good match was found between the simulated and measured characteristics, as illustrated by the solid lines in Figure 5 for the input irradiances of 81 mW cm^{-2} and 2 mW cm^{-2}. Normally the nonideal behavior of an organic photovoltaic is simulated by the addition of series and shunt resistances, R_s and R_{sh}, respectively, to the photocurrent source, I_{ph}, in parallel with a diode, D. We found that the experimental data could not be reproduced unless an additional pair of diodes, D_{bf} and D_{br}, with a second shunt resistance, R_b, is incorporated in the circuit to simulate a blocking contact. At high irradiance D_{br} becomes nonideal with an ideality factor of 1.9 to match the experimental data, so giving an asymmetric blocking contact. R_{sh} originates from continuous pathways for both electrons and holes between the anode and cathode. Recently Waldauf et al. have shown that $1/R_{sh}$ increases linearly with I_{in} since it is proportional to the density of photogenerated carriers.[45] As Figure 8 shows, $1/R_{sh}$ varies according to $I_{in}^{1.04}$, which is in reasonable agreement with the expected linear relationship. This suggests that the shunt resistance indeed originates from the active layer of the device. The series resistance, R_s, represents the bulk resistance of the layers and contact resistance between the layers and can be estimated from the slope of the current−voltage characteristics at high voltages. As expected from the high voltage slopes of Figure 5 and confirmed in the simulations, R_s varies by only a small amount, from 640 Ω cm^2 to 490 Ω cm^2, on increasing the input irradiance from 0.05 mW cm^{-2} to 80 mW cm^{-2}. This small variation with I_{in} implies that R_s is not dominated by the bulk resistance of the active organic layer but by other layers/interfaces in the device. However the absolute value of R_s is 2 orders of magnitude higher than that found in state of the art polymer-fullerene devices.[46,47] The asymmetric blocking contact and high R_s is responsible for the low fill factor at high irradiances. We believe that both of these parameters are not intrinsic to the device, since we have recently reduced the R_s of a similar device to 25 Ω cm^2 by modifying the processing conditions of the lower electrode. We simulated the photocurrent-voltage characteristics of device A with $I_{in} = 81$ mW cm^{-2} on removal of the blocking contact and with R_s equal to 4.7Ω cm^2, equal to that obtained in a state of the art polymer photovoltaic. A PCE of 1% is obtained as opposed to the measured value of 0.25%. Further improvements would also be expected by optimizing the spatial features of the porous network as discussed above. The amplitude of the pores of the porous networks presented here is deeper, 13 nm compared with 6.5 nm, than that prepared from the LC gel described elsewhere.[1] However the in-plane spatial features of the gel template are significantly finer than shown here, with spatial frequencies extending to 40 μm^{-1}. This may contribute to the higher PCE , 0.6% at 45 mW cm^{-2}, of the gel device although a direct comparison is not valid since different material combinations are used. We are currently synthesizing new materials with different polymerizable groups to enable faster cross-linking to give finer pore features.

IV. Conclusion

Liquid crystal composites provide a new approach to provide a distributed heterointerface between electron-donating and electron-accepting organic semiconductors in an organic photovoltaic. A distributed interface is preferred to a localized interface in a bilayer device, since it allows a greater fraction of photogenerated excitons to reach the interface before recombination and so assists charge generation. The interface is formed from an interpenetrating liquid crystal polymer network prepared using two distinct techniques. Coarser in-plane spatial features of the interface are correlated with poorer device performance, and further improvements in the dimensions of the network surface roughness are required to optimize the interface. We examine the photocurrent-voltage characteristics as a function of input irradiance. The monochromatic power conversion efficiency varies between 0.8% and 0.3%. We find that charge recombination is monomolecular in the interpenetrating bilayer devices but is partially bimolecular in a control blend device. The shunt resistance of the device originates from

(45) Waldauf, C.; Scharber, M. C.; Schilinsky, P.; Hauch, J. A.; Brabec, C. J. *J. Appl. Phys.* **2006**, *99*, 104503.
(46) Riedel, I.; Parisi, J.; Dyakonov, V.; Lutsen, L.; Vanderzande, D.; Hummelen, J. C. *Adv. Funct. Mater.* **2004**, *14*, 38.
(47) Schilinsky, P.; Waldauf, C.; Hauch, J.; Brabec, C. J. *J. Appl. Phys.* **2004**, *95*, 2816.

the active organic layer, which provides some continuous pathways for both electrons and holes between the anode and cathode. The high series resistance is extrinsic to the active layer of the device and can be removed with improved device processing. Liquid crystal composites are compatible with roll-to-roll processing and other high throughput manufacturing processes. This and the relatively high mobility of nematic liquid crystals should stimulate both academic and commercial interest in this new approach to organic photovoltaics and solar cells.

Acknowledgment. G. Sowersby is thanked for technical support. We acknowledge the EPSRC for financial support.

CM071727Q